Laboratory Studies of Molecular Growth in the Titan Ionosphere[†]

Roland Thissen,[‡] Veronique Vuitton,*,[‡] Panayotis Lavvas,[§] Joel Lemaire,[||] Christophe Dehon,[||] Odile Dutuit,[‡] Mark A. Smith,[§,⊥] Stefano Turchini,[#] Daniele Catone,[#] Roger V. Yelle,[‡,§] Pascal Pernot,[||] Arpad Somogyi,[⊥] and Marcello Coreno[▽]

Laboratoire de Planétologie de Grenoble, CNRS, Université J. Fourier, UMR 5109, Grenoble, France, Lunar and Planetary Laboratory, University of Arizona, Tucson, AZ, Laboratoire de Chimie Physique, CNRS, Université Paris-Sud, UMR 8000, Orsay, France, Department of Chemistry and Biochemistry, University of Arizona, Tucson, AZ, CNR-ISM, Roma, Italy, and CNR-IMIP & INFM-TASC, Elettra Sincrotrone, Trieste, Italy

Received: May 29, 2009; Revised Manuscript Received: July 31, 2009

Experimental simulations of the initial steps of the ion−molecule reactions occurring in the ionosphere of Titan were performed at the synchrotron source Elettra in Italy. The measurements consisted of irradiating gas mixtures with a monochromatic photon beam, from the methane ionization threshold at 12.6 eV, up to and beyond the molecular nitrogen dissociative ionization threshold at 24.3 eV. Three gas mixtures of increasing complexity were used: N_2/CH_4 (0.96/0.04), $N_2/CH_4/C_2H_2$ (0.96/0.04/0.001), and $N_2/CH_4/C_2H_2/C_2H_4$ (0.96/0.04/0.001/0.001). The resulting ions were detected with a high-resolution (1 T) FT-ICR mass spectrometer as a function of time and VUV photon energy. In order to interpret the experimental results, a Titan ionospheric model was adapted to the laboratory conditions. This model had previously allowed the identification of the ions detected in the Titan upper atmosphere by the ion neutral mass spectrometer (INMS) onboard the Cassini spacecraft. Comparison between observed and modeled ion densities validates the kinetic model (reactions, rate constants, product branching ratios) for the primary steps of molecular growth. It also reveals differences that we attribute to an intense surface chemistry. This result implies that heterogeneous chemistry on aerosols might efficiently produce HCN and NH_3 in the Titan upper atmosphere.

Introduction

Titan has been an object of considerable scrutiny since the arrival of Cassini−Huygens in the Saturn system in July 2004. Titan is the only satellite in the Solar System with an extensive atmosphere, largely composed of N_2, with CH_4 (2%) and H_2 (0.4%) being the most abundant minor constituents.[1,2] A plethora of hydrocarbons,[3,4] nitrogen-bearing species,[5] and oxygen-bearing species[6] complete the collection of compounds that exist in Titan's atmosphere.

The Cassini measurements have shown the upper atmosphere to be the key to understanding the complex chemical evolution on Titan. It is the region where solar extreme ultraviolet (EUV) and soft-X-ray radiation interact with the main atmospheric constituents, thus initiating high-energy neutral and ion gas phase chemistry more complex than anticipated and found on any other planet. The Cassini ion neutral mass spectrometer (INMS) has detected positively charged hydrocarbons and nitrogen-bearing species with a mass-to-charge ratio (m/z) reaching 100 amu,[7,8] the upper limit of the m/z range of the instrument. Data from the ion beam spectrometer of the Cassini plasma spectrometer (CAPS-IBS) have moreover revealed the presence of much heavier positive ions with masses of hundreds

of amu.[9] The electron spectrometer (CAPS-ELS) observed negative ions with typically $m/z = 10−50$ amu but also m/z values of up to 10 000 amu.[10,11]

These observations revealed that a good description of Titan's ion chemistry is crucial for our understanding of not only Titan's upper atmosphere but also the whole aerosol formation process. Vuitton et al.[12] suggested that proton exchange reactions drive the chemistry and that the most abundant ions are essentially protonated neutrals (closed-shell ions). They attributed the previously nonattributed ions at even m/z as protonated species bearing a single atom of nitrogen. Moreover, by coupling a zero-dimensional chemical model with the measured densities of ions, they inferred the abundance of 19 neutral species at 1100 km, most of them not having previously been observed on Titan.

Carrasco et al.[13,14] performed the first detailed uncertainty analysis concerning the kinetics parameters of the ion−molecule reactions included in a Titan ionospheric chemistry model. They showed that uncertainty on measured branching ratios as well as reaction list incompleteness regarding both the differential reactivity of isomers and heavy ion ($m/z > 50$) production are the limiting factors for accurate ion density prediction. Thus, in order to improve the accuracy of photochemical models, specific laboratory measurements of rate constants and product branching ratios have to be performed.[15] However, acquiring data for hundreds of reactions is an extensive work and many years will be required to achieve such a task. Another approach consists of performing "global" laboratory simulations aimed at reproducing some specific mechanisms identified as being important for the chemical growth in Titan's atmosphere.

Many laboratory simulations relevant to the chemistry occurring at all levels of Titan's atmosphere have been performed. In order to reproduce the ionospheric chemistry occurring in

the upper atmosphere, an energy source able to ionize N_2 and CH_4 is required. Typically, a N_2–CH_4 gas mixture is ionized into a plasma and the neutral products produced after some time of irradiation are collected and analyzed by mass spectrometry.[16–18] However, plasma discharges tend to induce poorly controlled high-energy processes as they produce a tail of hot electrons as well as ultraviolet light. Thus, the representativeness of these energy sources is questionable. Ultraviolet lamps have also been used as an energy source, but these experiments focused on the neutral chemistry occurring in Titan's stratosphere.[19,20] Although hydrocarbons containing two carbon atoms are present in Titan's upper atmosphere at the 100 ppm level, they have never been included in the initial gas mixture of plasma experiments. These species are some of the major irradiation products and should as a consequence be largely involved in the subsequent chemistry, but a specific study of their impact on the chemical growth has never been performed.

Only recently Imanaka and Smith[21] investigated the formation of gas species from N_2–CH_4 as a function of irradiation wavelength using synchrotron light (8–25 eV). A clear increase in the formation of complex species and especially aromatics is observed at energies over 15.6 eV, which corresponds to the ionization threshold of N_2. As only neutral molecules were analyzed in this work, it was not possible to determine the complete role of ion chemistry in driving the complex reaction pathways. These results were obtained with low-resolution undulator light ($E/\Delta E$ of about 40), and the possible interference of dissociative ionization threshold such as CH_2^+ and CH_3^+ from CH_4 (15.2 and 14.3 eV, respectively) could not be excluded, calling for new measurements with improved photon energy resolution.

In order to further refine information on the first steps of the ion–molecule chemistry in these processes, we present here a novel experiment performed inside the trap of a Fourier transform ion cyclotron resonance (FT-ICR) mass spectrometer. Gas mixtures representative of Titan's atmospheric composition were injected inside the FT-ICR cell and irradiated using extreme ultraviolet (EUV) radiation from the Elettra synchrotron. The evolution of the ions with time was followed *in situ* for various gas concentrations as the irradiation energy was scanned over the (dissociative) ionization thresholds of the reactant gases. Three different gas mixtures of increasing complexity were used in order to specifically study the impact of C2 hydrocarbons on the molecular growth. The experimental results are compared to the predictions from a model of the chemistry in the ion trap based on the Vuitton et al.[12] reaction list. This approach allows constraining the model predictions against the laboratory experiments and to test for missing and/or poorly constrained pathways.

Experimental Methods

1. MICRA. MICRA, the compact, rugged, and easily transportable FT-ICR prototype used in this work,[22,23] is especially well suited for short period runs at a Synchrotron light source, where users' space and time accessibility are restricted. On the basis of a 1.25 T permanent magnet, it avoids many constraints linked to cryogenic superconducting magnets in commercial FT-ICR machines, while preserving an ultimate mass resolution $m/\Delta m$ better than 73 000 at $m/z = 132$.[24] Figure 1 represents MICRA and the ion trap located inside a cylindrical vacuum chamber fitting into the 5 cm diameter bore of the magnet. The trap is a cubic cell with internal dimensions $2 \times 2 \times 2$ cm^3. Rather than using grids, two opposite side electrodes are replaced by sets of four interconnected electrodes (called
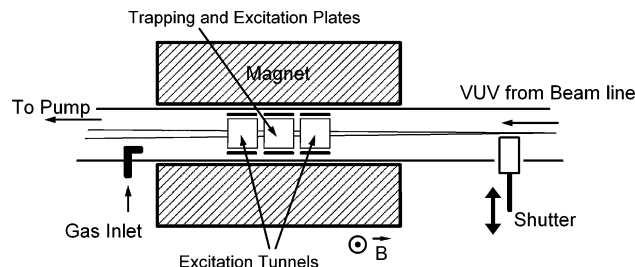

Figure 1. Scheme of MICRA as used in the context of these measurements.

"tunnels") so that the light beam can cross the trap without interacting with surfaces.

Primary ions are generated in the cell by photoionization of gas mixtures admitted through a pulsed valve. Ions are produced all along the light path, but only those produced in the central region of the cell (within about 6 mm from the cell center in Figure 1) are trapped. Resonant excitation of the ion cyclotron motion is obtained by applying a radio frequency signal on excitation plates. Ions orbiting between the detection plates induce an image current signal, which is Fourier transformed to give the mass spectrum.

It is generally assumed that ICR cells can trap ions up to the space charge limit, which is typically 10^6 ions·cm^{-3}. Following the same trend, it is assumed that the detection electronics are able to amplify and positively detect a bunch of 100 charges moving coherently inside the cell. The detection dynamics of this type of instrument is therefore limited to 4 orders of magnitude at most, putting constraints on the detectability of minor species. In order to circumvent this limitation, we developed a strategy of multiple spectra acquisition and averaging: (i) averaging of 30 transient signals during data acquisition, (ii) averaging of all spectra in a range of energy where no ionization or dissociation threshold was expected in order to confirm the detection of otherwise faint signals.

In order to check the correlation between signal intensity and number of ions, natural CCl_4 was ionized with 70 eV electrons. The base peak in the spectrum corresponds to the different isotopologues of CCl_3^+ with expected intensity ratios 1000:958:306:33 (Table S1 in the Supporting Information). The peak at 121 amu is about 40% smaller than the expected intensity, and the peak at mass 123 was never observed. It is not clear to us what is responsible for this discrepancy. As a consequence, we will consider our data as semiquantitative only; i.e., a positive detection is always valid, but the absence of detection might often be due to the limited sensitivity.

2. Elettra, CIPO Beamline. The experiments were performed at the circular polarization beamline[25] at the Elettra synchrotron radiation facility (Trieste, Italy). The normal incidence monochromator with a 2400 grooves·mm^{-1} Au coated grating was used, covering the photon energy range from 5 to 35 eV. The highest flux is at 21 eV (Figure S2 in the Supporting Information), and the design ensures removal of the second-order photons above 14 eV.

During all measurements, entrance and exit slits were opened at 200 μm, which ensures an energy resolving power $E/\Delta E$ better than 500 over the full energy range, i.e., sufficient for our experimental objectives. The flux is estimated to be in the range of 10^{12} photons·s^{-1} at a photon energy of 21 eV with an operating storage ring current of 200 mA and an energy of 2.0 GeV. The monochromator was calibrated during the measurement session, using the molecular nitrogen features in the vicinity of its ionization threshold. The photon energy accuracy
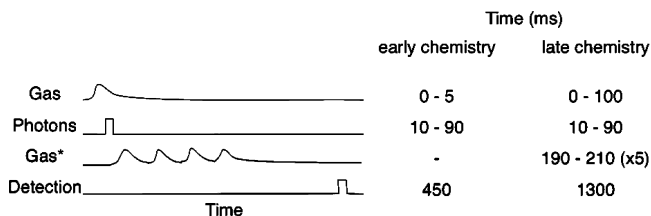
Molecular Growth in the Titan Ionosphere

J. Phys. Chem. A, Vol. 113, No. 42, 2009 **11213**

Figure 2. Timing of gas injection, irradiation, and detection.

is better than 4 meV in the full energy range. As the insertion device is an undulator (roughly 1.5 eV fwhm bandwidth), a collaborative mode of the monochromator and undulator was designed in order to have the optimal photon flux at each point in the energy scan.

3. Experimental Description. The timing of a typical experimental sequence is shown in Figure 2. The gas mixture is pulsed into the FT-ICR cell and irradiated with monochromatic EUV photons from the CIPO beamline. Up to five short gas pulses are subsequently added in order to maintain a base pressure large enough to enhance molecular growth. The background gas is pumped, and the ion motion is coherently excited and detected. A set of 30 sequences of this kind is averaged in order to increase the signal-to-noise ratio of the mass spectrum. This leads to roughly 5 h duration for the energy scan, an optimum considering the signal stability and the necessity to measure three different gas mixtures during the allocated beam time. Although many gas pulse sequences have been tested, we will specifically focus on two of them. The first one probes the "early" chemistry, i.e., the primary ions produced directly by irradiation with reduced chemistry, and the second one probes the "late" chemistry, i.e., the ions produced after 1.3 s. The timing of these specific sequences is detailed in Figure 2.

The experiments were performed at a pressure of about 4×10^{-5} mbar, as measured with a Bayard Alpert ionization gauge, and confirmed by the quantitative model developed to interpret the data (see kinetic modeling). This pressure corresponds to an altitude of about 750 km on Titan, about 300 km lower than the altitude of the ionospheric peak. This pressure was optimum to observe the maximum of molecular size increase, i.e., the highest number of subsequent reactive collisions. At this pressure, three-body reactions are not effective (see kinetic modeling). Experimental constraints did not allow us to cool down the reaction cell to Titan's temperature (150 K), and the temperature was approximately 300 K. The temperature effect on the branching ratios of ion−molecule reactions can substantially affect the ion distribution,[13] and this issue needs to be addressed in future studies.

Three gas mixtures (Linde, research grade, 99.995%) with N_2, CH_4 (mixture A), and minor amounts of C_2H_2 (mixture B) and C_2H_4 (mixture C) were used (Table 1). These mixtures are representative of the composition of Titan's upper atmosphere, although the mixing ratio of CH_4, C_2H_2, and C_2H_4 in our mixtures is enhanced by comparison to the Titan mixing ratios[3,12] to accelerate the production of heavier species. Energy scans were performed in the range 13.5−26.5 eV with a scan step of 0.1 eV. Moreover, some "kinetics-like" scans were recorded by changing the gas injection time in the cell from a single gas pulse of 5 ms to multiple gas pulses adding up to 200 ms, while keeping the detection time constant (1200 ms). This approach allows probing the evolution of the chemistry with reaction time.

Prior to experiments, the reaction chamber was baked out at a temperature of 120 °C for 18 h. This produced a base pressure

TABLE 1: Gas Mixing Ratios in the Three Mixtures Used in This Experiment

gas mixture	mixing ratio				
	N_2	CH_4	C_2H_2	C_2H_4	density (cm^{-3})
A	9.6×10^{-1}	4.0×10^{-2}			1.0×10^{12}
B	9.6×10^{-1}	4.0×10^{-2}	1.0×10^{-3}		1.0×10^{12}
C	9.6×10^{-1}	4.0×10^{-2}	1.0×10^{-3}	1.0×10^{-3}	1.0×10^{12}
Titan[a]	9.8×10^{-1}	1.8×10^{-2}	1.3×10^{-4}[b]		4.8×10^9

[a] Globally averaged mixing ratios on Titan at 1025 km altitude.[3] [b] Linear combination of C_2H_2 and C_2H_4 densities in the form of $(3n(C_2H_2) + n(C_2H_4))/4$.

of 5×10^{-8} mbar, most of which was likely caused by the degassing of H_2O adsorbed on all of the surfaces of the chamber and the gas inlet manifold.[20,26] This background signal slowly diminished during the following days. Our best measurements (reduced signal of water and concomitantly longest reaction times) were hence performed during the last 48 h of the allocated beam time.

According to these considerations, spectra always contain some amount of water signature: either H_2O^+ ($m/z = 18.010$) or H_3O^+ ($m/z = 19.018$) when ions were stored for longer times. Fortunately, the mass resolution of the instrument was sufficient to positively detect NH_4^+ at $m/z = 18.034$. The water was included in the kinetic modeling of the experiments.

4. Data Analysis. The data sets were deconvoluted by Fourier transform (FFT) to frequency spectra. The mass (m/z) associated to each frequency f can be derived with the approximate equation:

$$m = m_{ref} \left(\frac{f_c + f_m}{f} - \frac{f_c \times f_m}{f^2} \right) \qquad (1)$$

where m_{ref} is the m/z of H_3O^+ (19.01784) and the cyclotron and magnetron frequencies (f_c and f_m, about 991 and 3 kHz, respectively) are derived from the position of two intense peaks in the spectra (H_3O^+ and either N_2^+ or $HCNH^+$). Calibration of each spectra was performed, and ionic species could be searched for, at better than 100 ppm of their theoretical m/z.

A total of 57 potential ionic species ranging from N^+ to $C_6H_7^+$ were systematically searched for in the data sets. The list of the ions that have been positively detected in mixtures A, B, and C is presented in Table 2. Further information that was derived from each spectrum is the average noise level, and its variance, in order to ascertain the peak assignment uncertainty. A typical mass spectrum obtained with this procedure is presented in Figure 3. The peaks with the same nominal mass, N_2^+/$HCNH^+$/$C_2H_4^+$ at $m/z = 28$ are clearly separated. The dynamic range in this spectrum is slightly better than 10^2.

Kinetic Modeling

In order to validate our current knowledge for the photochemistry of the involved species, we compare the measured ion abundances with a zero-dimensional photochemical model that solves the time-dependent continuity equation for the concentration of ions in the cell. The model is specifically designed for the simulation of the experimental procedure and takes into account the number and duration of the gas pulses, the irradiation time, and also the contribution of neutral species from the surface residue.

1. Neutral Gases. The density of the neutral gases in the cell is variable due to the continuous pumping, and its magnitude depends on the duration of the gas pulses. The evolution of the

11214 *J. Phys. Chem. A, Vol. 113, No. 42, 2009*

Thissen et al.

TABLE 2: List of Ionic Species That Have Been Positively Detected in Mixtures A (N_2/CH_4), B ($N_2/CH_4/C_2H_2$), and C ($N_2/CH_4/C_2H_2/C_2H_4$), as Well as Their m/z

ion[a]	m/z	mixture A	mixture B	mixture C
N^+	14.003	X		X
CH_2^+	14.015	X		X
CH_3^+	15.023	X	X	X
CH_4^+	16.031	X		X
CH_5^+	17.039	X	X	X
H_2O^+	18.010	X	X	X
NH_4^+	18.034	X	X	X
H_3O^+	19.018	X	X	X
$C_2H_2^+$	26.015		X	X
$C_2H_3^+$	27.023			X
N_2^+	28.006	X	X	X
$HCNH^+$	28.018	X	X	X
$C_2H_4^+$	28.031	X	X	X
N_2H^+	29.013	X	X	X
$C_2H_5^+$	29.039	X	X	X
CH_2OH^+	31.018	X	X	X
$C_2H_7^+$	31.054		X	
$C_3H_3^+$	39.023		X	X
$C_3H_4^+$	40.031			X
$C_3H_5^+$	41.039		X	X
$C_2H_7O^+$	47.049	X		
$C_4H_5^+$	53.039		X	X
$C_5H_5^+$	65.039		X	X

[a] Other ion species that were searched for but not detected include NH^+, NH_2^+, OH^+, NH_3^+, C_2^+, C_2H^+, CN^+, HCN^+, CHO^+, CH_3N^+, CH_4N^+, $C^{13}CH_5^+$, $C_2H_6^+$, $CH_3OH_2^+$, C_3^+, C_3H^+, $C_2H_2N^+$, $C_2H_3N^+$, N_3^+, $C_2H_4N^+$, C_3N^+, $C_4H_2^+$, HC_3N^+, $C_4H_3^+$, HC_3NH^+, $C_2H_3CN^+$, $C_2H_3CNH^+$, $C_2H_5CN^+$, $C_4H_7^+$, $C_2H_5CNH^+$, $C_5H_7^+$, $C_5H_9^+$, $C_6H_6^+$, and $C_6H_7^+$.
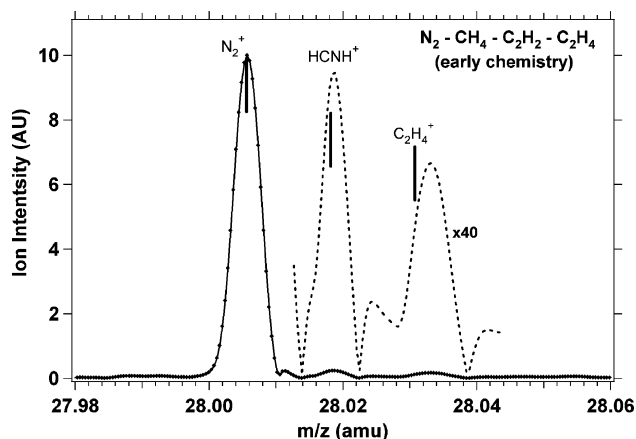
Figure 3. Close-up of a typical mass spectrum around $m/z = 28$. The vertical solid lines represent the theoretical m/z of each ion.

total density in the system can be described by the continuity equation:

$$\frac{\partial n}{\partial t} = P - Ln \tag{2}$$

where n is the total density at time t, $P(t)$ the production rate (cm^{-3} s^{-1}) of neutrals in the cell as a function of time, and L the loss rate (s^{-1}) due to the pumping and the photoionization. Under the conditions of the experiment, the latter loss process is much smaller than the pumping rate and can be neglected.

In order to identify the characteristic times for each process (gas bursts and pumping), we performed separate calibration measurements for the identification of the pulse structure. The

TABLE 3: Ionization Thresholds of N_2, CH_4, C_2H_2, and C_2H_4 between 10 and 26.5 eV

products	threshold[a] (eV)	products	threshold[a] (eV)
N_2		CH_4	
$N_2^+(X)$	15.6	CH_4^+	12.6
$N_2^+(A)$	16.7	$CH_3^+ + H$	14.3
$N_2^+(B)$	18.8	$CH_2^+ + H_2$	15.2
$N^+(^3P) + N(^4S)$	24.3	$CH^+ + H_2 + H$	19.9
$N^+(^1D) + N(^4S)$	26.2		
C_2H_2		C_2H_4	
$C_2H_2^+$	11.4	$C_2H_4^+$	10.5
$C_2H^+ + H$	17.3	$C_2H_2^+ + H_2$	13.1
$CH_2^+ + C$	19.4	$C_2H_3^+ + H$	13.3
$CH^+ + CH$	20.7	$CH_3^+ + CH$	17.0
$C^+ + ...?$	21.2	$CH^+ + CH_3$	17.7
		$CH_2^+ + CH_2$	17.8
		$C_2H^+ + H_2 + H$	18.7
		$C^+ + ...?$	24.4
		$C_2^+ + ...?$	24.5

[a] From NIST, rounded to the above 0.1 eV, corresponding to the step of our photon energy scans.

output of an ionization gauge was recorded for a pressure varying from 10^{-6} to 5×10^{-4} mbar and pulse duration varying from 5 to 1000 ms. The profile obtained for a pressure of 7.5 $\times 10^{-5}$ mbar and a first pulse of 100 ms followed by four pulses of 20 ms every 100 ms is presented in Figure S1 in the Supporting Information. There is a time lag between the opening of the valve and the onset of the increase in pressure, corresponding to the time the gas takes to reach the cell. The pressure stays constant within about 15% as the secondary gas pulses are injected. Finally, after the last pulse, it takes about 100 ms for the gas to totally exit the cell. The pressure decrease should be close to an exponential with a slope depending on the volume and the pumping speed. This behavior is observed for short gas pulses but not for long ones. This is explained by a decrease in the gauge linearity. We simulated the gas production rate assuming that each gas burst can be described by a specific structure function that depends on the duration of the pulse followed by an exponential decay of characteristic time, τ_{burst}. The calculated density profile for the case of a typical gas burst sequence is presented in Figure S1 in the Supporting Information. The magnitude of the production rate was scaled so that the resulting maximum density in the cell corresponds to a specific maximum pressure that is an input parameter to the calculations. In order to parametrize the pumping loss rate, we use a characteristic time for pumping:

$$L = -\frac{\ln(0.5)}{\tau_{pump}} \tag{3}$$

On the basis of this parametrization, we deduce that the delay time for the gas to reach the cell is 50 ms, the characteristic time for the burst is $\tau_{burst} = 25$ ms, and the characteristic time for pumping is $\tau_{pump} = 110$ ms.

2. Kinetics. The cross sections for the ionization of neutral species are taken from Carter, Samson et al., and Stolte et al.[27−29] for N_2, Lee and Chiang and Samson et al.[30,31] for CH_4, Hayaishi et al. and Suto and Lee[32,33] for C_2H_2, and Holland et al.[34] for C_2H_4. The (dissociative) ionization thresholds of these same four molecules are listed in Table 3. The ion-neutral chemical reaction rates are taken from Vuitton et al.[12] They are used for the analysis of the INMS data and are considered to be the state of the art, in our current knowledge of ion reactions in

Molecular Growth in the Titan Ionosphere

J. Phys. Chem. A, Vol. 113, No. 42, 2009 **11215**

N_2-CH_4-hydrocarbon mixtures, such as the one in Titan's atmosphere. We have included both two-body and three-body reactions in our calculations, since the latter could be important if the total pressure in the cell reached high values. After the validation of the model with the measurements and the retrieval of the real pressure in the cell, addition of three-body reactions was found to be unnecessary. Due to the experimental design, the electrons formed during the photoionization are not trapped in the cell. Hence, recombination reactions were not considered in the calculations.

3. Energy Spectrum. The ions produced in the cell during the ionization process are trapped up to a maximum density that depends on the Coulomb repulsion between the ions. In this experiment, the cell approaches saturation when the number of ions reaches 10^6. Also, the photon flux provided by the synchrotron depends on the photon energy as presented in Figure S2 in the Supporting Information. Comparing the ion intensity in the energy scans with the photon flux reveals that, when the photon flux is maximum (18−25 eV), the number of ions in the cell is no longer proportional to the photon flux, suggesting that the cell approaches saturation. Since we do not have absolute measurements for the extent of the ion loss, we apply an empirical correction factor to the photon flux in order to correct for this effect in the simulations. The photon flux eventually applied in the model calculations in order to take into account the saturation effect in the ion trapping efficiency is presented in Figure S2 in the Supporting Information.

Results and Discussion

1. Mass Spectra. Mass spectra obtained at $E_{h\nu} = 26.5$ eV for the "late" chemistry sequence are presented in Figure 4a,b,c for mixtures A, B, and C, respectively. In the three mixtures, the highest intensity peak is H_3O^+ at $m/z = 19$. This peak is explained by the presence of residual H_2O in the FT-ICR cell, as detailed in the Experimental Methods section. Other ions formed by irradiation of gas mixture A are NH_4^+, $HCNH^+$, $C_2H_4^+$, and $C_2H_5^+$ (Figure 4a). These ions cannot be formed from direct ionization of N_2 and CH_4, and their presence is the evidence for ion−molecule reactions occurring in the FT-ICR cell. However, the heaviest detected species do not have more than two C and/or N atoms, indicating that the molecular growth is very limited. When C_2H_2 is included in the initial gas mixture (mixture B), three new ions are detected and are attributed to $C_3H_3^+$, $C_3H_5^+$, and $C_4H_5^+$ (Figure 4b). The presence of these heavier ions indicates that the addition of C_2H_2 to the reactant gas mixture opens new pathways, leading to more complex species. Finally, when both C_2H_2 and C_2H_4 are included (mixture C), the same ions are detected but the intensity of $C_3H_5^+$ increases by about 1 order of magnitude (Figure 4c). This is the sign that the presence of C_2H_4 opens a new channel, leading to $C_3H_5^+$.

Figure 4d presents the mass spectrum obtained for the "early" chemistry sequence, for mixture C and at $E_{h\nu} = 26.5$ eV. Seven other ions are detected: CH_3^+, CH_5^+, H_2O^+, $C_2H_2^+$, $C_2H_3^+$, N_2^+, and N_2H^+. These are light species, suggesting that, with this sequence, we are indeed probing the primary reactions occurring in the cell. The ions detected here are very likely the precursors of the ions detected with the "late" chemistry sequence.

2. Energy Scans. A photon energy scan from 13 to 26.5 eV for the "late" chemistry sequence and mixture C is presented in Figure 5a. All of the ions with a detectable intensity are plotted on the graph. The overall evolution of the ion intensity with photon energy depends on the ionization cross section of the reactant neutrals and on the flux of the synchrotron radiation (Figure S2 in the Supporting Information). H_3O^+, the most
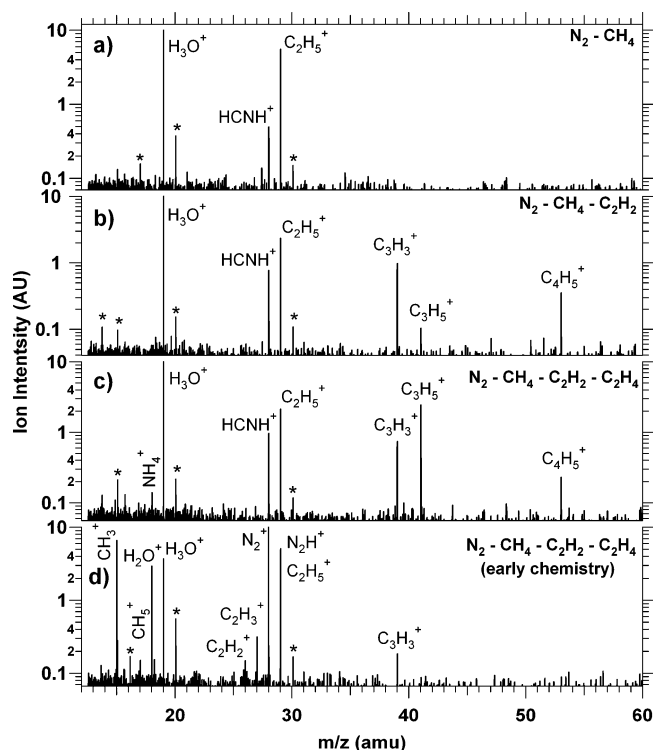

Figure 4. Mass spectra obtained at $E_{h\nu} = 26.5$ eV: (a) "late" chemistry sequence and gas mixture A, N_2/CH_4; (b) "late" chemistry sequence and gas mixture B, $N_2/CH_4/C_2H_2$; (c) "late" chemistry sequence and gas mixture C, $N_2/CH_4/C_2H_2/C_2H_4$; (d) "early" chemistry sequence and gas mixture C, $N_2/CH_4/C_2H_2/C_2H_4$. All mass spectra have been recorded with the high resolution shown in Figure 3, which allows the separation of N_2H^+ and $C_2H_5^+$, for example. The peaks labeled with * correspond to interferences.

abundant ion, is detected at all photon energies, while $C_2H_5^+$ and $C_3H_5^+$ appear around 14.5 eV. The sharp increase in the ion densities at 15.6 eV corresponds to the ionization threshold of N_2 (Table 3), and the structure in the ion intensity around 16 eV clearly correlates with the predissociation levels of N_2. These features indicate that N_2^+ plays a crucial role in the production of the ions detected, consistent with the observations of Imanaka and Smith.[21] The intensity of most of the ions presents a smooth decrease above 23 eV, corresponding to the decrease of the photon flux (Figure S2 in the Supporting Information). However, both nitrogen-bearing ions, NH_4^+ and $HCNH^+$, have a constant or slightly increasing intensity in this region. The dissociative ionization threshold of N_2 (Table 3) is at 24.3 eV, suggesting that chemistry related with N^+ has some impact on the density of these ions. We will return to this in more detail in the chemical production and loss subsection.

3. "Kinetics-Like" Scans. In order to obtain "kinetics-like" scans, the gas injection time, i.e., the amount of gas injected, was changed stepwise, while the gas mixture, photon energy, and duration and detection time were kept constant. The ion intensities for a set of gas pulse trains obtained for mixture B at the energy of 24.3 eV is presented in Figure 6b,c. The main ions, H_3O^+ and $C_2H_5^+$, as well as $C_2H_4^+$ are fairly constant with the amount of gas injected. However, the density of CH_3^+, H_2O^+, N_2^+, and N_2H^+ decreases sharply as the amount of gas increases and becomes lower than the detection limit when the injection time is longer than 50 ms. Those species have already been identified in the "early" chemistry spectrum in Figure 4d. Their behavior confirms that they are primary species that react to form heavier species as the quantity of neutral gas in the FT-ICR cell is increased. Indeed, the density of several ions
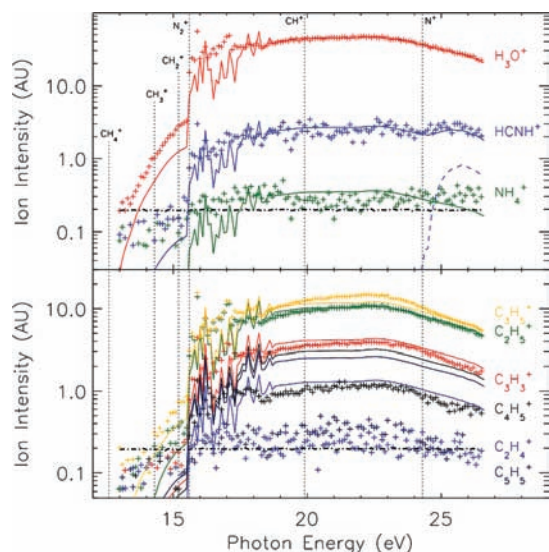
Figure 5. Energy scan from 13 to 26.5 eV, for mixture C (N_2/CH_4/C_2H_2/C_2H_4) and the "late chemistry" sequence. The dot–dashed line represents the ion detection limit. The vertical dotted lines represent the formation thresholds of various ions. (a) The crosses represent the experimental intensity of H_3O^+, NH_4^+, and $HCNH^+$. The dashed lines represent the model predictions with no HCN and no NH_3. In this case, the model produces virtually no NH_4^+ and some $HCNH^+$ is only produced for photon energies above 15.6 eV. The thick solid lines represent the model predictions with 10^8 cm^{-3} H_2O, 10^7 cm^{-3} HCN, and 10^6 cm^{-3} NH_3. (b) The crosses represent the experimental intensity of six hydrocarbon ions, and the solid lines represent the model predictions. The model ion densities have all been scaled by a common factor for the measured and simulated H_3O^+ to match with each other.
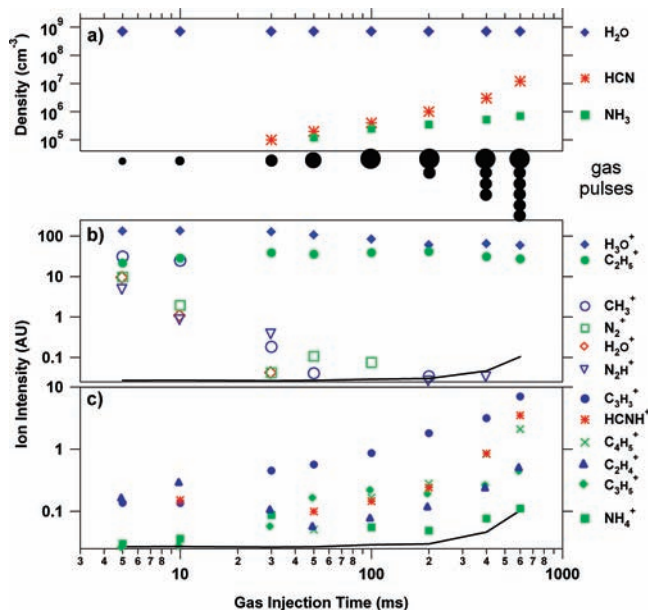

Figure 6. "Kinetics-like" scan for mixture B (N_2/CH_4/C_2H_2) and photon irradiation energy of 24.3 eV. The gas injection time ranges from a primary pulse of 5 ms to a primary pulse of 100 ms followed by five secondary pulses of 20 ms, as indicated by the size of the black dots. (a) Density of H_2O, HCN, and NH_3 required in the cell to fit the H_3O^+, $HCNH^+$, and NH_4^+ intensity. (b and c) Ion intensity (AU). The solid line represents the ion detection limit.

increases with the gas injection time: $HCNH^+$, $C_3H_3^+$, $C_3H_5^+$, and $C_4H_5^+$. Again, these ions have been identified in the "late" chemistry spectra and are the result of substantial molecular growth in the cell.

4. Ion Mole Fractions Predicted by the Model. In this section, we compare the measured ion abundances to the theoretical predictions of the photochemical model. The most important reactions to describe the observed ions are included in Table S2 in the Supporting Information and will be discussed in the next section. The predicted ion mole fractions as a function of irradiation energy for mixture C and the "late" chemistry sequence are presented in Figure 5. The intensity of H_3O^+ at all photon energies can be reproduced with a H_2O density inside the cell of 10^8 cm^{-3}. Because of the loss in detection efficiency for the low-intensity ions, the model predictions are scaled to the measurements for easier comparison. The simulated H_3O^+ density is scaled to the observed intensity of H_3O^+ at 23 eV (in the smooth part of the measurements), while the simulated density ratio between H_3O^+ and the other ions is kept constant.

The model predicts the presence, with a relative intensity above 1%, of the six hydrocarbon ions detected experimentally. The calculated and experimental appearance threshold are in good agreement for all hydrocarbon ions. Especially, the model predicts the density of $C_2H_5^+$ and $C_3H_5^+$ to become higher than the detection limit between 14.5 and 15 eV, in good agreement with the experimental trend. Moreover, the relative densities of the three most abundant hydrocarbon ions, $C_2H_5^+$, $C_3H_3^+$, and $C_3H_5^+$, are in excellent agreement with the observed intensities. The three less abundant hydrocarbon ions, $C_2H_4^+$, $C_4H_5^+$, and $C_5H_5^+$, are predicted with relative densities up to 1 order of magnitude higher than observed. This is consistent with the observation that the detection efficiency in the FT-ICR is not linear and that low-intensity ions are systematically underestimated. The model does not predict the presence of any other ions with a relative intensity higher than 1%.

Both NH_4^+ and $HCNH^+$ are observed experimentally at 15.6 eV for all three gas mixtures, while our model fails to predict the formation of any nitrogen-bearing species but N_2^+ at this energy. Hence, through ion-neutral chemistry, the direct production of NH_4^+ and $HCNH^+$ requires N^+ ions in the medium, i.e., photon energies above 24.3 eV. Various hypotheses can be made about the process at the origin of this discrepancy:

(i) Reaction induced dissociation of N_2^+? Since their formation is correlated with the formation of N_2^+ and this even when only N_2 and CH_4 are present in the mixture, the simplest explanation would be that unknown reaction between N_2^+ and CH_4 produces some N+. However, this reaction has been extensively studied (Nicolas et al.[35] and references therein), and it is clear that it leads exclusively to the dissociative charge transfer (N_2^+ + CH_4 → CH_x^+ + H_{4-x} + N_2).

(ii) Reactivity of N_2^+ excited states? The threshold of N_2^+(A) and N_2^+(B) is 16.7 and 18.9 eV, respectively, which is higher than the appearance threshold of NH_4^+ and $HCNH^+$.

(iii) Two-photon process? Above 12.1 eV, photodissociation of N_2 occurs and atomic nitrogen is produced up to 18.8 eV. Although not trapped in the cell, the atoms could be ionized by a second photon to produce N^+ ions and further ion growth to $HCNH^+$ or NH_4^+ could occur. The density of photons on the synchrotron beamline is however far too low to consider such a mechanism.

(iv) Proton transfer? A final hypothesis to produce NH_4^+ and $HCNH^+$ is through proton exchange reactions with NH_3 and HCN. Since both species have a high proton affinity (713 and 854 kJ/mol, respectively), they will readily abstract a proton from any of the closed-shell ions
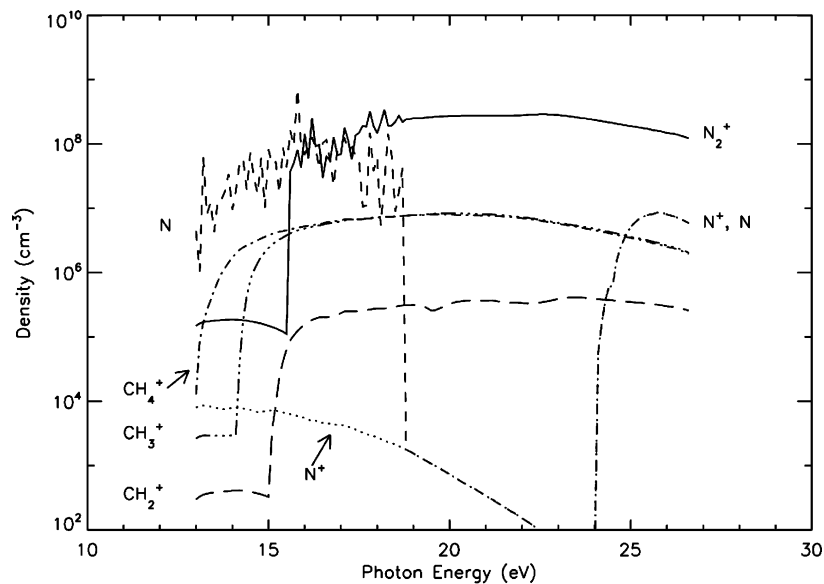
Molecular Growth in the Titan Ionosphere

J. Phys. Chem. A, Vol. 113, No. 42, 2009 **11217**

Figure 7. Density of ions (CH_4^+, CH_3^+, CH_2^+, N_2^+, N^+) and N atoms created from N_2 and CH_4 photoionization and photodissociation as a function of photon energy, using the retrieved gas and photon pulse profiles and assuming no loss of species (chemistry or pumping). Second-order photons are taken into account in the calculations.

present in the FT-ICR cell, including H_3O^+. In this case, the origin of neutrals can be multiple:

(a) Neutral atom reactivity? The atomic radicals generated by photolysis are formed in the $N(^4S)$ and $N(^2D)$ state, of which $N(^2D)$ is known to react with CH_4 and eventually produces HCN. The argument against this hypothesis is first kinetic (rate and densities are too slow/low to account for the signals) and second thermodynamic: the threshold for this process is below 15.5 eV and it should disappear above 19 eV, in disagreement with our observations.

(b) Memory effect? The instrument was carefully cleaned and baked before the measurement session. Pyridine and a pyrimidine type of molecules were studied earlier in the same instrument, but their protonated species, though feasible, were never observed. Memory effects are usually visible when introducing in an instrument molecules of same or similar polarity; here, we introduced exclusively nonpolar N_2 and CH_4, and it is therefore difficult to invoke the release of NH_3 and HCN during the pulse train.

(c) Surface induced production? This hypothesis is to us the most likely and will be detailed in the next section.

5. Surface Effects. We have used the set of pulse trains in order to retrieve some information regarding the density and the temporal evolution of the NH_3 and HCN densities in the cell. About 10^6 cm^{-3} NH_3 and 10^7 cm^{-3} HCN are required in order to match the measured NH_4^+ and $HCNH^+$ densities, as shown in Figure 6a. Simulation of the abundance of the NH_4^+ and $HCNH^+$ signals for different pulse trains requires the use of different densities for the two gases in the cell with increasing values for larger pulse durations (Figure 6a). This suggests that HCN and NH_3 observed through their protonated ions are not present in the cell in a constant density, as is the case with H_2O, but instead there is a local (in time) production which increases with increasing neutral gas density. There are two possible options to explain this behavior. Either the increasing neutral gas density is causing the release of molecules from the surface of the cell due to collisions, or there is a chemical process producing these molecules at the surface. Due to the small

densities and velocities of the neutrals in the cell, we anticipate that the first case would have a minor effect, suggesting that a chemical process catalyzed by the presence of the surface is responsible for our observations.

Figure 7 presents the density of primary ions formed in the photolysis of N_2–CH_4, based on the photon flux and the neutral density. The calculations include both the first and second order of the monochromator. The second order is conservatively assumed to correspond to a flux 1000 times smaller than the first order. A large number of neutral nitrogen atoms are formed at energies below the N_2^+ threshold, while above the ionization threshold of N_2, the products are dominated by N_2^+. The neutral N formed is not trapped in the cell and hence can directly interact with the surface where it can be deposited. On the other hand, the N_2^+ formed can be trapped up to the saturation limit of the cell due to the coulomb repulsion of the ions. The excess ions are quickly lost along the magnetic field lines, toward the trapping plates. With a limit of $\sim10^6$ ions in the cell and a typical number of N_2^+ formed larger than 8×10^8 ions, the number of N_2^+ ions escaping is significant. At the same time, the photolysis of CH_4 releases also neutral carbon and hydrogen in multiple forms (CH_3, CH_2, H, etc.), which can also interact with the nitrogen present on the surface and lead to the production of HCN and NH_3. The model is also able to reproduce the rise in $HCNH^+$ density at the N^+ formation threshold, as discussed in the chemical production and loss subsection. The real density of these species is probably a factor of a few higher because of the loss in detection sensitivity for the less intense ions (see the Experimental Methods section).

6. Chemical Production and Loss. The experimental evolution of the ions with time and energy can be explained by a set of formation and loss reactions, as inferred from the model. The principal production and loss reactions of the ions detected experimentally are listed in Table S2 in the Supporting Information and are presented in Figure 8. Although Vuitton et al.[12] introduced in their reaction list a number of proton exchange reactions with rate constants assumed equal to the collisional rate, all of the reactions included in Table S2 in the Supporting Information have been studied experimentally. The main chemical processes leading to the formation of the ions and their subsequent chemistry are further detailed hereafter. These
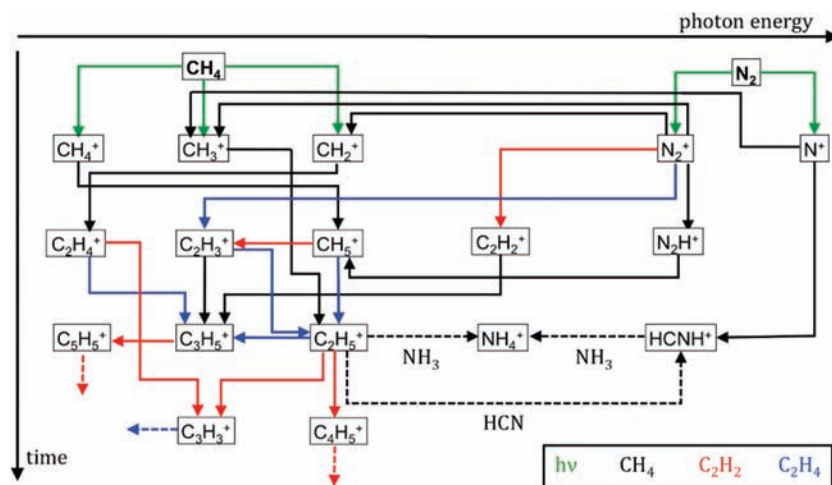
Figure 8. Chemical flowchart representing the most important reactions taking place in the FT-ICR cell, according to the chemical model.

processes are consistent with the observations, as can be inferred from the good agreement between observed and predicted ion densities in Figure 5.

Between the photon energy of 12.6 and 14.3 eV, the only primary ion is CH_4^+, which can subsequently react with CH_4 to produce CH_5^+ (k_1). The latter does not react with CH_4 and is the terminal ion. Between 14.3 and 15.2 eV, photoionization of CH_4 leads to production of CH_3^+ as well as CH_4^+. CH_3^+ reacts with CH_4 to produce $C_2H_5^+$ (k_2), which does not react any further with CH_4. Above 15.2 eV, a third channel opens in the photoionization of CH_4, leading to the formation of CH_2^+. Again, CH_2^+ reacts with CH_4 to produce $C_2H_4^+$ (k_3) but the latter does not react any further with CH_4.

Above 15.6 eV, photons are energetic enough to ionize N_2. N_2^+ reacts with CH_4, producing both CH_3^+ (k_4) and CH_2^+ (k_5), as well as N_2H^+ (k_6). The latter can subsequently react with CH_4 to form CH_5^+ (k_7). Thus, ionization of N_2 leads only to the formation of one single new product: N_2H^+. However, because N_2 is so much more abundant than CH_4 (96/4%) while their ionization cross sections are of the same order of magnitude, the number of ions created increases by a factor of about 25, as expected from the ratio of densities (Figure 7). This gives a false feeling of more complex chemistry: the same ions as for a pure CH_4 mixture are present, with the exception of N_2H^+. The presence of NH_4^+ and $HCNH^+$ can only be explained by the presence of NH_3 and HCN in the gas phase and subsequent proton transfer reactions ($k_8–k_{10}$). Hence, photoionization of a $N_2–CH_4$ mixture leads to a limited set of products, the heaviest ones being $C_2H_5^+$ and $HCNH^+$.

Above 24.3 eV, dissociative photoionization of N_2 takes place and the reaction of N^+ with CH_4 produces both CH_3^+ (k_{11}) and $HCNH^+$ (k_{12}). The opening of this new channel for production of $HCNH^+$ explains the little bump in the $HCNH^+$ intensity around 25–26 eV. In the same way, the production of N^+ above the threshold can lead to the production of NH^+ by reaction with H_2 and CH_4. The same reactions can further produce NH_2^+ and NH_3^+ and eventually yield NH_4^+. Yet, although we detect this sequence in the model results, the predicted NH_4^+ relative intensity is extremely small relative to the detected value, suggesting that a different process is responsible for the production of this ion below and above the N_2 dissociative ionization threshold. We then suggest that formation of ambient NH_3 by wall chemistry followed by proton transfer produces NH_4^+, as discussed in the Surface Effects section.

When C_2H_2 is present in the gas mixture, a whole set of new reactions opens up as all of the terminal hydrocarbon ions in

the presence of N_2 and CH_4 alone can now react with C_2H_2. CH_5^+ produces $C_2H_3^+$ (k_{13}), which reacts with CH_4 to form $C_3H_5^+$ (k_{14}), which reacts itself with C_2H_2 to form $C_5H_5^+$ (k_{15}). The reaction of both $C_2H_4^+$ (k_{16}) and $C_2H_5^+$ (k_{17}) with C_2H_2 produces $C_3H_3^+$, while the reaction of $C_2H_5^+$ also forms $C_4H_5^+$ (k_{18}). Finally, the reaction of N_2^+ with C_2H_2 produces $C_2H_2^+$ (k_{19}) that is quickly transformed to $C_3H_5^+$ (k_{20}). Thus, the chemical complexity is greatly enhanced when C_2H_2 is added to the gas mixture with six new hydrocarbon ions being produced.

When C_2H_4 is added to the previous gas mixture, the same ions are formed but the intensity of $C_3H_5^+$ increases because of new reaction pathways leading to this ion: the reaction of $C_2H_4^+$ with C_2H_4 (k_{21}), the reaction of N_2^+ with C_2H_4 to form $C_2H_3^+$ (k_{22}) followed by its reaction (k_{23}), as well as the reaction of CH_5^+ (k_{24}) with C_2H_4 to form $C_2H_5^+$, ending with reaction of the latter with C_2H_4 to form $C_3H_5^+$ (k_{25}).

Throughout the experiments, H_3O^+ is formed by proton transfer reactions from CH_5^+ (k_{26}) and $C_2H_5^+$ (k_{27}) to H_2O and lost by proton transfer to $HCNH^+$ (k_{28}). H_2O^+ is produced by charge transfer of N_2^+ to H_2O (k_{29}) and quickly reacts with CH_4 and C_2H_2 to produce H_3O^+ (k_{30}) and $C_2H_2^+$ (k_{31}), respectively. Thus, H_2O^+ and H_3O^+ are intermediates in the chemistry of interest here and do not lead to the formation of further oxygen-bearing species.

In order to highlight the basic chemistry responsible for the rich ionospheric composition observed in Titan's atmosphere, Carrasco et al.[14,36] performed extensive studies on the reactions necessary to reproduce the INMS mass spectrum ($m/z < 50$) measured at 1200 km during the T5 flyby. Out of the 700 ion–molecule reactions constituting their database, they found that only 35 reactions are required to reproduce this reference mass spectrum (Tables 2 and 3, and Figure 5 in ref 36). It is striking to see that 22 out of the 31 reactions that are important to reproduce the laboratory experiments (Table S2 in the Supporting Information) are also necessary to reproduce the INMS ion spectrum. Only reactions k_9, k_{10}, k_{18}, k_{21}, k_{23}, k_{26}, k_{29}, k_{30}, and k_{31} are not required to reproduce the INMS spectrum, most likely because of the lower concentrations of NH_3, C_2H_4, and H_2O in Titan's atmosphere. This strong overlap between both data sets is clear evidence that the experiment is representative of the first chemical steps occurring in Titan's ionosphere.

The reactions listed in Table S2 in the Supporting Information include six proton exchanges to the three neutral species that have the highest proton affinity: NH_3 (k_9, k_{10}), HCN (k_8, k_{28}),

Molecular Growth in the Titan Ionosphere

J. Phys. Chem. A, Vol. 113, No. 42, 2009 **11219**

and H_2O (k_{26}, k_{27}). This suggests that, although condensation reactions dominate the chemistry for hydrocarbons that generally have a low proton affinity, for nitrogen- and oxygen-bearing species, proton transfer is the dominant mechanism. This is consistent with the suggestion of Vuitton et al.[12] that the reactivity of nitrogen-bearing species in Titan's ionosphere is mainly driven by proton exchange reactions. However, experimental studies of these reactions are required in order to definitely validate the dominant processes.

Conclusions

We performed laboratory simulations and compared the results obtained to the predictions of a theoretical model in order to better characterize the primary ion−molecule reactions taking place in Titan's upper atmosphere. We followed the evolution in a FT-ICR of about 20 ions with time and irradiation energy for three different gas mixtures. We detected more complex ions when C_2H_2 and/or C_2H_4 are present at the 10^{-3} level in a N_2−CH_4 mixture. We also observed a clear increase in the chemical growth above the N_2 ionization threshold, in agreement with Imanaka and Smith.[21] We interpret this as an increase of the number of ions produced because of the higher mixing ratio of N_2 compared to CH_4 in the gas mixture. N_2^+ mostly acts as a catalyst in the dissociation of CH_4 to produce more hydrocarbon ions, either directly or via N_2H^+, but does not directly initiate the formation of any carbon- and nitrogen-bearing species. However, N^+ reacts with CH_4 to form $HCNH^+$. The most complex ions observed experimentally are $C_4H_5^+$ and $C_5H_5^+$, formed by three consecutive ion−molecule reactions. These ions can engage in further reactions with C_2H_2 and C_2H_4, but the limited dynamic range of the FT-ICR combined with the presence of H_3O^+ as the major ions precludes one from detecting heavier species.

Because of the loss of sensitivity of the instrument for minor ions, only semiquantitative information on the ion mixing ratios could be retrieved. As a consequence, it was not possible to directly compare the predicted ion densities with the experimental results. Instead, we focused on the relative evolution of the ion intensities with irradiation energy and injection time. Within these limits, the experimental and theoretical trends were found to be consistent with each other for all detected hydrocarbon ions, thus validating the reaction scheme presented here. The model predicted all of the ions observed experimentally with a relative intensity higher than 1%. In turn, all of the hydrocarbon ions predicted by the model with a relative intensity higher than 1% were observed experimentally. The only exceptions are NH_4^+ and $HCNH^+$ that are detected above the N_2 ionization threshold, while the model predicts their formation above the N_2 dissociative ionization threshold only. We believe that these ions are formed by proton exchange reactions to NH_3 and HCN that are formed by heterogeneous reactions on the walls of the instrument. This result raises the question of the importance of heterogeneous chemistry in previous laboratory simulations.

Although the mole fraction of NH_3 has been inferred to be 7×10^{-6} at 1100 km,[12] photochemical models predict its abundance to be less than 2×10^{-7} and an efficient process leading to this molecule is clearly missing.[37−39] NH_3 is ubiquitous in the interstellar medium where it is formed on grain surfaces by consecutive addition of H atoms onto NH.[40] H and NH radicals are readily available in the upper atmosphere of Titan.[37] Data from CAPS-ELS show some evidence for the presence at 1000 km of negative ions with m/z up to 10 000 amu and maybe higher.[10] This corresponds to a particle radius

of about 3 nm, assuming a density of 1 g·cm^{-3}. As a consequence, an interesting possibility is the formation of NH_3 on the surface of aerosol seeds in Titan's atmosphere.

Supporting Information Available: Table S1 showing the relative intensities of the four major ions present in the mass spectrum of CCl_4. Table S2 showing the principal production and loss reactions for the ions detected experimentally. Figure S1 showing a comparison between the measured and simulated gas density variation with time. Figure S2 showing the variation of the Elettra photon flux with photon energy and the flux variation eventually applied in the model calculations after inclusion of saturation effects in the ion trapping efficiency. This material is available free of charge via the Internet at http://pubs.acs.org.

References and Notes

(1) Flasar, F. M.; Achterberg, R. K.; Conrath, B. J.; Gierasch, P. J.; Kunde, V. G.; Nixon, C. A.; Bjoraker, G. L.; Jennings, D. E.; Romani, P. N.; Simon-Miller, A. A.; Bézard, B.; Coustenis, A.; Irwin, P. G. J.; Teanby, N. A.; Brasunas, J.; Pearl, J. C.; Segura, M. E.; Carlson, R. C.; Mamoutkine, A.; Schinder, P. J.; Barucci, A.; Courtin, R.; Fouchet, T.; Gautier, D.; Lellouch, E.; Marten, A.; Prangé, R.; Vinatier, S.; Strobel, D. F.; Calcutt, S. B.; Read, P. L.; Taylor, F. W.; Bowles, N.; Samuelson, R. E.; Orton, G. S.; Spilker, L. J.; Owen, T. C.; Spencer, J. R.; Showalter, M. R.; Ferrari, C.; Abbas, M. M.; Raulin, F.; Edgington, S.; Ade, P.; Wishnow, E. H. *Science* **2005**, *308*, 975.
(2) Yelle, R. V.; Borggren, N.; De La Haye, V.; Kasprzak, W. T.; Niemann, H. B.; Müller-Wodarg, I. C. F.; Waite, J. H., Jr. *Icarus* **2006**, *182*, 567.
(3) Cui, J.; Yelle, R. V.; Vuitton, V.; Waite, J. H., Jr.; Kasprzak, W. T.; Gell, D. A.; Niemann, H. B.; Müller-Wodarg, I. C. F.; Borggren, N.; Fletcher, G. G.; Patrick, E. L.; Raaen, E.; Magee, B. *Icarus* **2009**, *200*, 581.
(4) Vinatier, S.; Bézard, B.; Fouchet, T.; Teanby, N. A.; de Kok, R.; Irwin, P. G. J.; Conrath, B. J.; Nixon, C. A.; Romani, P. N.; Flasar, F. M.; Coustenis, A. *Icarus* **2007**, *188*, 120.
(5) Teanby, N. A.; Irwin, P. G. J.; de Kok, R.; Nixon, C. A.; Coustenis, A.; Bézard, B.; Calcutt, S. B.; Bowles, N. E.; Flasar, F. M.; Fletcher, L.; Howett, C.; Taylor, F. W. *Icarus* **2006**, *181*, 243.
(6) De Kok, R.; Irwin, P. G. J.; Teanby, N. A.; Lellouch, E.; Bézard, B.; Vinatier, S.; Nixon, C. A.; Fletcher, L.; Howett, C.; Calcutt, S. B.; Bowles, N. E.; Flasar, F. M.; Taylor, F. W. *Icarus* **2007**, *186*, 354.
(7) Waite, J. H., Jr.; Niemann, H. B.; Yelle, R. V.; Kasprzak, W. T.; Cravens, T. E.; Luhmann, J. G.; McNutt, R. L., Jr.; Ip, W.-H.; Gell, D.; De La Haye, V.; Müller-Wodarg, I. C. F.; Magee, B.; Borggren, N.; Ledvina, S. A.; Fletcher, G. G.; Walter, E. M.; Miller, R.; Scherer, S.; Thorpe, R. L.; Xu, J.; Block, B. P.; Arnett, K. *Science* **2005**, *308*, 982.
(8) Cravens, T. E.; Robertson, I. P.; Waite, J. H., Jr.; Yelle, R. V.; Kasprzak, W. T.; Keller, C. N.; Ledvina, S. A.; Niemann, H. B.; Luhmann, J. G.; McNutt, R. L., Jr.; Ip, W.-H.; De La Haye, V.; Müller-Wodarg, I. C. F.; Wahlund, J.-E.; Anicich, V.; Vuitton, V. *Geophys. Res. Lett.* **2006**, *33*, L07105.
(9) Waite, J. H., Jr.; Young, D. T.; Cravens, T. E.; Coates, A. J.; Crary, F. J.; Magee, B.; Westlake, J. *Science* **2007**, *316*, 870.
(10) Coates, A. J.; Crary, F.; Lewis, G.; Young, D. T.; Waite, J. H., Jr.; Sittler, E. C. J. *Geophys. Res. Lett.* **2007**, *34*, L22103.
(11) Coates, A. J.; Wellbrock, A.; Lewis, G. R.; Jones, G. H.; Young, D. T.; Crary, F. J.; Waite, J. H., Jr. *Planet. Space Sci.*, in press.
(12) Vuitton, V.; Yelle, R. V.; McEwan, M. J. *Icarus* **2007**, *191*, 722.
(13) Carrasco, N.; Alcaraz, C.; Dutuit, O.; Plessis, S.; Thissen, R.; Vuitton, V.; Yelle, R. V.; Pernot, P. *Planet. Space Sci.* **2008**, *56*, 1644.
(14) Carrasco, N.; Dutuit, O.; Thissen, R.; Banaszkiewicz, M.; Pernot, P. *Planet. Space Sci.* **2007**, *55*, 141.
(15) McEwan, M. J.; Anicich, V. G. *Mass Spectrom. Rev.* **2007**, *26*, 281.

(16) Coll, P.; Coscia, D.; Smith, N.; Gazeau, M.-C.; Ramirez, S. I.; Cernogora, G.; Israel, G.; Raulin, F. *Planet. Space Sci.* **1999**, *47*, 1331.

(17) Fujii, T.; Arai, N. *Astrophys. J.* **1999**, *519*, 858.

(18) Thompson, W. R.; Henry, T. J.; Schwartz, J. M.; Khare, B. N.; Sagan, C. *Icarus* **1991**, *90*, 57.

(19) Tran, B. N.; Joseph, J. C.; Force, M.; Briggs, R. G.; Vuitton, V.; Ferris, J. P. *Icarus* **2005**, *177*, 106.

(20) Vuitton, V.; Doussin, J.-F.; Bénilan, Y.; Raulin, F.; Gazeau, M.-C. *Icarus* **2006**, *185*, 287.

(21) Imanaka, H.; Smith, M. A. *Geophys. Res. Lett.* **2007**, *34*, L02204.

(22) Lemaire, J.; Boissel, P.; Heninger, M.; Mauclaire, G.; Bellec, G.; Mestdagh, H.; Simon, A.; Le Caër, S.; Ortega, J.-M.; Glotin, F.; Maître, P. *Phys. Rev. Lett.* **2002**, *89*, 273002.

(23) Maître, P.; Le Caër, S.; Simon, A.; Jones, W.; Lemaire, J.; Mestdagh, H.; Heninger, M.; Mauclaire, G.; Boissel, P.; Prazeres, R.; Glotin, F.; Ortega, J.-M. *Nucl. Instrum. Methods Phys. Res., Sect. A* **2003**, *507*, 541.

(24) Mauclaire, G.; Lemaire, J.; Boissel, P.; Bellec, G.; Heninger, M. *Eur. J. Mass Spectrom.* **2004**, *10*, 155.

(25) Desiderio, D.; DiFonzo, S.; Diviacco, B.; Jark, W.; Krempasky, J.; Krempaska, R.; Lama, F.; Luce, M.; Mertins, H. C.; Piacentini, M.; Prosperi, T.; Rinaldi, S.; Soullie, G.; Schäfers, F.; Schmolle, F.; Stichauer, L.; Turchini, S.; Walker, R. P.; Zema, N. *Synchrotron Radiat. News* **1999**, *12*, 34.

(26) Tran, B. N.; Ferris, J. P.; Chera, J. J. *Icarus* **2003**, *162*, 114.

(27) Carter, V. *J. Chem. Phys.* **1972**, *56*, 4195.

(28) Samson, J. A. R.; Masuoka, T.; Pareek, P. N.; Angel, G. C. *J. Chem. Phys.* **1987**, *86*, 6128.

(29) Stolte, W. C.; He, Z. X.; Cutler, J. N.; Lu, Y.; Samson, J. A. R. *At. Data Nucl. Data Tables* **1998**, *69*, 171.

(30) Lee, L. C.; Chiang, C. C. *J. Chem. Phys.* **1983**, *78*, 688.

(31) Samson, J. A. R.; Haddad, G. N.; Masuoka, T.; Pareek, P. N.; Kilcoyne, D. A. L. *J. Chem. Phys.* **1989**, *90*, 6925.

(32) Hayaishi, T.; Iwata, S.; Sasanuma, M.; Ishiguro, E.; Morioka, Y.; Iidat, Y.; Nakamura, M. *J. Phys. B: At. Mol. Opt. Phys.* **1982**, *15*, 79.

(33) Suto, M.; Lee, L. C. *J. Chem. Phys.* **1984**, *80*, 4824.

(34) Holland, D. M. P.; Shaw, D. A.; Hayes, M. A.; Shpinkova, L. G.; Rennie, E. E.; Karlsson, L.; Baltzer, P.; Wannberg, B. *Chem. Phys.* **1997**, *219*, 91.

(35) Nicolas, C.; Torrents, R.; Gerlich, D. *J. Chem. Phys.* **2003**, *118*, 2723.

(36) Carrasco, N.; Plessis, S.; Dobrijevic, M.; Pernot, P. *Int. J. Chem. Kinet.* **2008**, *40*, 699.

(37) Krasnopolsky, V. A. *Icarus* **2009**, *201*, 226.

(38) Lavvas, P.; Coustenis, A.; Vardavas, I. M. *Planet. Space Sci.* **2008**, *56*, 67.

(39) Wilson, E. H.; Atreya, S. K. *J. Geophys. Res.* **2004**, *109*, E06002.

(40) Lequeux, J. *The interstellar medium*; Springer: Berlin, 2005.

JP9050353